



High-precision Transition Energy Measurements of Neon-like Fe XVII Ions

Chintan Shah^{1,2,3} , Moto Togawa^{2,4,5} , Marc Botz^{2,5} , Jonas Danisch² , Joschka J. Goes² , Sonja Bernitt^{2,6,7,8} ,
Marleen Maxton² , Kai Köbnick² , Jens Buck⁹ , Jörn Seltmann¹⁰ , Moritz Hoesch¹⁰ , Ming Feng Gu¹¹ ,
F. Scott Porter¹ , Thomas Pfeifer² , Maurice A. Leutenegger¹ , Charles Cheung¹² , Marianna S. Safronova¹² , and
José R. Crespo López-Urrutia²

¹ NASA Goddard Space Flight Center, 8800 Greenbelt Road, Greenbelt, MD 20771, USA

² Max-Planck-Institut für Kernphysik, Saupfercheckweg 1, 69117 Heidelberg, Germany; chintan.shah@mpi-hd.mpg.de

³ Center for Space Sciences and Technology, University of Maryland, Baltimore County, 1000 Hilltop Circle, Baltimore, MD 21250, USA

⁴ European XFEL, Holzkoppel 4, 22869 Schenefeld, Germany

⁵ Heidelberg Graduate School of Fundamental Physics, Ruprecht-Karls-Universität Heidelberg, Im Neuenheimer Feld 226, 69120 Heidelberg, Germany

⁶ GSI Helmholtzzentrum für Schwerionenforschung, Planckstraße 1, 64291 Darmstadt, Germany

⁷ Helmholtz-Institut Jena, Fröbelstieg 3, 07743 Jena, Germany

⁸ Institut für Optik und Quantenelektronik, Friedrich-Schiller-Universität, Max-Wien-Platz 1, 07743 Jena, Germany

⁹ Institut für Experimentelle und Angewandte Physik, Christian-Albrechts-Universität zu Kiel, Kiel, Germany

¹⁰ Deutsches Elektronen-Synchrotron (DESY), Notkestraße 85, 22607 Hamburg, Germany

¹¹ Space Science Laboratory, University of California, Berkeley, CA 94720, USA

¹² Department of Physics and Astronomy, University of Delaware, Newark, DE 19716, USA

Received 2024 January 11; revised 2024 April 2; accepted 2024 April 28; published 2024 June 28

Abstract

We improve by a factor of 4–20 the energy accuracy of the strongest soft X-ray transitions of Fe XVII ions by resonantly exciting them in an electron beam ion trap with a monochromatic beam at the P04 beamline of the PETRA III synchrotron facility. By simultaneously tracking instantaneous photon-energy fluctuations with a high-resolution photoelectron spectrometer, we minimize systematic uncertainties down to 10–15 meV, or velocity equivalent $\pm \sim 5 \text{ km s}^{-1}$ in their rest energies, substantially improving our knowledge of this key astrophysical ion. Our large-scale configuration-interaction computations include more than 4 million relativistic configurations and agree with the experiment at a level without precedent for a 10-electron system. Thereby, theoretical uncertainties for interelectronic correlations become far smaller than those of quantum electrodynamics (QED) corrections. The present QED benchmark strengthens our trust in future calculations of many other complex atomic ions of interest to astrophysics, plasma physics, and the development of optical clocks with highly charged ions.

Unified Astronomy Thesaurus concepts: Atomic data benchmarking (2064); Laboratory astrophysics (2004); Line positions (2085); Atomic spectroscopy (2099); Experimental data (2371); Theoretical techniques (2093); Space plasmas (1544)

1. Introduction

Over the past three decades, extensive research has focused on the soft X-ray emission from Ne-like iron (Fe XVII, Fe¹⁶⁺), particularly in hot astrophysical plasmas observed by Chandra and XMM-Newton (Behar et al. 2001; Brinkman et al. 2001). The dominant spectral transitions $3d \rightarrow 2p$ and $3s \rightarrow 2p$ of Fe XVII within the 700–850 eV range (14.5–17.5 Å) play a crucial role in deducing the plasma parameters across various sources. These parameters include the electron temperature, density, elemental abundance, gas motion, and photon scattering opacity (Parkinson 1973; Smith et al. 1985; Schmelz et al. 1992; Waljeski et al. 1994; Phillips et al. 1996; Behar et al. 2001; Mauche et al. 2001; Doron & Behar 2002; Xu et al. 2002; Gu 2003; Paerels & Kahn 2003; Werner et al. 2009; Pradhan & Nahar 2011; Beiersdorfer et al. 2018; Gu et al. 2019, 2020; Grell et al. 2021).

Despite decades of study, since early solar X-ray observations (Parkinson 1973; Smith et al. 1985; Schmelz et al. 1992; Waljeski et al. 1994), discrepancies between observed and theoretical intensity ratios (Brown et al. 1998) have persisted.

Early explanations invoking resonance scattering (McKenzie et al. 1980; Schmelz et al. 1992; Saba et al. 1999) found no confirmation in measurements with electron-beam ion traps (EBITs) and tokamaks that also agreed with solar observations (Brown et al. 1998, 2001a, 2001b; Beiersdorfer et al. 2002, 2004; Brown et al. 2006; Gillaspay et al. 2011; Beiersdorfer et al. 2017; Shah et al. 2019). As optically thin laboratory plasmas are not subject to resonance scattering, indirect line formation mechanisms were suggested (Chen & Pradhan 2002; Gu 2003; Beiersdorfer et al. 2008, 2014, 2015; Shah et al. 2019; Gu et al. 2020; Grilo et al. 2021). An experiment with a free-electron laser aimed at directly determining the oscillator-strength ratio for lines 3C and 3D without uncertainties due to electron-impact excitation. Its unexpected results departing even more from theory were attributed to inaccuracies in calculated oscillator strengths (Bernitt et al. 2012), but soon after, unforeseen transient nonequilibrium effects and population transfer due to the ultrabright peak photon flux explained them (Oreshkina et al. 2014; Loch et al. 2015; Oreshkina et al. 2016; Wu & Gao 2019). Our later measurements (Kühn et al. 2020) with synchrotron radiation avoided this nonlinear systematic and improved the accuracy of the oscillator-strength ratio while still disagreeing with the theory. Finally, further increases in resolving power and signal-to-noise ratio found the cause of the persistent discrepancies in hitherto unresolvable

line wings and diffraction effects and brought the oscillator-strength ratio in line with state-of-the-art predictions (Kühn et al. 2022).

In spite of these advances, many questions remain open for this essential ion and many other less-studied species. For instance, widely used wavelength references for Fe XVII from EBIT measurements using a crystal spectrometer with a resolving power of 500–700 have uncertainties of 1–3 mÅ (~ 40 –200 meV), Doppler-equivalent to ~ 15 –50 km s $^{-1}$, i.e., ~ 60 –180 parts per million (ppm), for $n = 3 - 2$, and double that for high- n transitions (Beiersdorfer & Wargelin 1994; Brown et al. 1998). This is only marginally adequate for analysis of high-resolution diffraction grating spectra acquired with the Chandra High Energy Transmission Grating Spectrometer (HETGS), which can measure velocities of bright emission lines with ~ 25 km s $^{-1}$ systematic uncertainty (Ishibashi et al. 2006; Bozzo et al. 2023). These uncertainties in transition energies will also impair the achievement of the science goals of other extant, upcoming, and proposed missions, including XMM-Newton (den Herder et al. 2001; Jansen et al. 2001), XRISM (Tashiro et al. 2018), Athena (Barret et al. 2016; Pajot et al. 2018), Line Emission Mapper (LEM; Kraft et al. 2022), Arcus (Heilmann et al. 2022; Smith et al. 2022), and Lynx (Schwartz et al. 2019). Even though some of these missions feature spectrometers with FWHM resolution far broader than the uncertainties of published rest-energy determinations, well-exposed spectra of bright objects with a high signal-to-noise ratio will allow centroid determination with uncertainties comparable to or smaller than these prior measurements. There is clearly a need for better determinations of the Fe XVII transition energies that will allow us to take full advantage of the resolving power of current and future missions, as well as improved and well-benchmarked theoretical methods that can provide energies for transitions that have not yet been measured with sufficient precision.

We report new measurements of the rest energies of key Fe XVII transitions with an EBIT at the P04 beamline of the PETRA III synchrotron with uncertainties below 15 ppm, an improvement by a factor of 4–20 over the status quo. The accuracy of our results translates in velocity terms to 5 km s $^{-1}$ and fully unlocks the value of archived and forthcoming observations from XMM-Newton and Chandra, as well as of accurate velocimetry targeted by upcoming missions (Barret et al. 2016; Pajot et al. 2018; Heilmann et al. 2022; Kraft et al. 2022; Smith et al. 2022). We also test the large-scale configuration interaction (CI) approach and, therefore, our combination of the CI and coupled-cluster approaches (CI + all-order method), which is crucial for the development of high-precision clocks (Kozlov et al. 2018) and essential for understanding the quantum electrodynamics (QED) effects in many-electron systems. By applying the model potential approach (Tupitsyn et al. 2016) using the QEDMOD package (Shabaev et al. 2018), we incorporate QED effects into the effective Hamiltonian, basis-set orbitals, and one-electron matrix elements—a widely employed practice. The quality of the QED model potential is usually assessed against exact solutions for H-like ions since the uncertainty in the electronic correlation in HCI with a few valence electrons is usually larger, or at the level of QED contributions unless the ionization degree is rather high. Until this work, there were no

estimates regarding the accuracy of the QEDMOD approach for the majority of many-electron systems.

Motivated by our highly accurate experimental results, we carry out new CI computations, taking the contributions from high nl states into account, increasing the number of relativistic configurations from 1.2 million in our previous work (Cheung et al. 2021; Kühn et al. 2022) to over 4 million, and investigating the convergence of the computations in both of these parameters. The results show a remarkable degree of numerical convergence across all energy levels and agree with the measurements to a level of 1–33 meV (1–45 ppm) that is unprecedented for a complex ion such as Fe XVII. For the first time, uncertainties in the electronic correlations smaller than QED corrections allow us to test the accuracy of the QED contribution in a many-electron system.

2. Measurements and Data Analysis

PolarX-EBIT (Micke et al. 2018) was designed for the study of highly charged ions interacting with X-ray photons at synchrotrons and free-electron lasers (see Kühn et al. 2020; Leutenegger et al. 2020; Togawa et al. 2020; Kühn et al. 2022; Steinbrügge et al. 2022; Stierhof et al. 2022). Its off-axis electron gun emits a nearly monoenergetic electron beam that is compressed to a diameter of less than 100 μm by a magnetic field of ~ 870 mT generated by permanent magnets. Considering the overlap of the ion cloud and the electron beam leads to an effective electron density of $\sim 10^{10}$ cm $^{-3}$. Iron pentacarbonyl (Fe(CO) $_5$) molecules enter the trap region as a tenuous beam through a two-stage differential pumping system. There, electron-impact dissociation generates Fe atoms, and step-wise electron-impact ionization produces highly charged ions that remain radially trapped by the ensuing negative space-charge potential of the electron beam, and axially by biased cylindrical drift tubes. We chose operating conditions to ensure that Fe XVII ions mostly populate the trap.

At the soft X-ray beamline P04, an APPLE II undulator (Viefhaus et al. 2013) produces circularly polarized photons, which are then sent through a monochromator equipped with a variable line-spacing grating of 1200 lines mm $^{-1}$ mean groove density. Using an exit slit opening of 50 μm , the energy resolution ΔE was set to a value of approximately $E/\Delta E \approx 13,000$ in the energy range of 700–1100 eV. A pair of plane-elliptical mirrors refocus this beam onto the ion cloud. The photon beam energy is scanned over the Fe XVII transitions of interest and the corresponding calibration lines. Two silicon drift detectors (SDD) mounted at the top and on the side of the EBIT register fluorescence, with ~ 100 eV FWHM resolution, following from resonant photoexcitation as well as electron-impact excitation.

To calibrate the monochromator photon-energy scale, we excite K-shell transitions in H-like and He-like oxygen, fluorine, and neon ions trapped in PolarX-EBIT. Their energies can be calculated with uncertainties well below 1 meV. We take values for the H-like $1s \rightarrow 2p$ transitions from Yerokhin & Shabaev (2015), and from Erickson (1977) for $1s \rightarrow np$ up to $n = 7$, and for He-like ions, we take energy values from Yerokhin & Surzhykov (2019) for $1s \rightarrow np$ transitions up to $n = 7$.

The monochromator disperses the spectrum of the undulator cone on the exit slit by choice of incidence and diffraction angles of the grating, which is accomplished by appropriate rotations of both the grating and mirror, with the extra degree

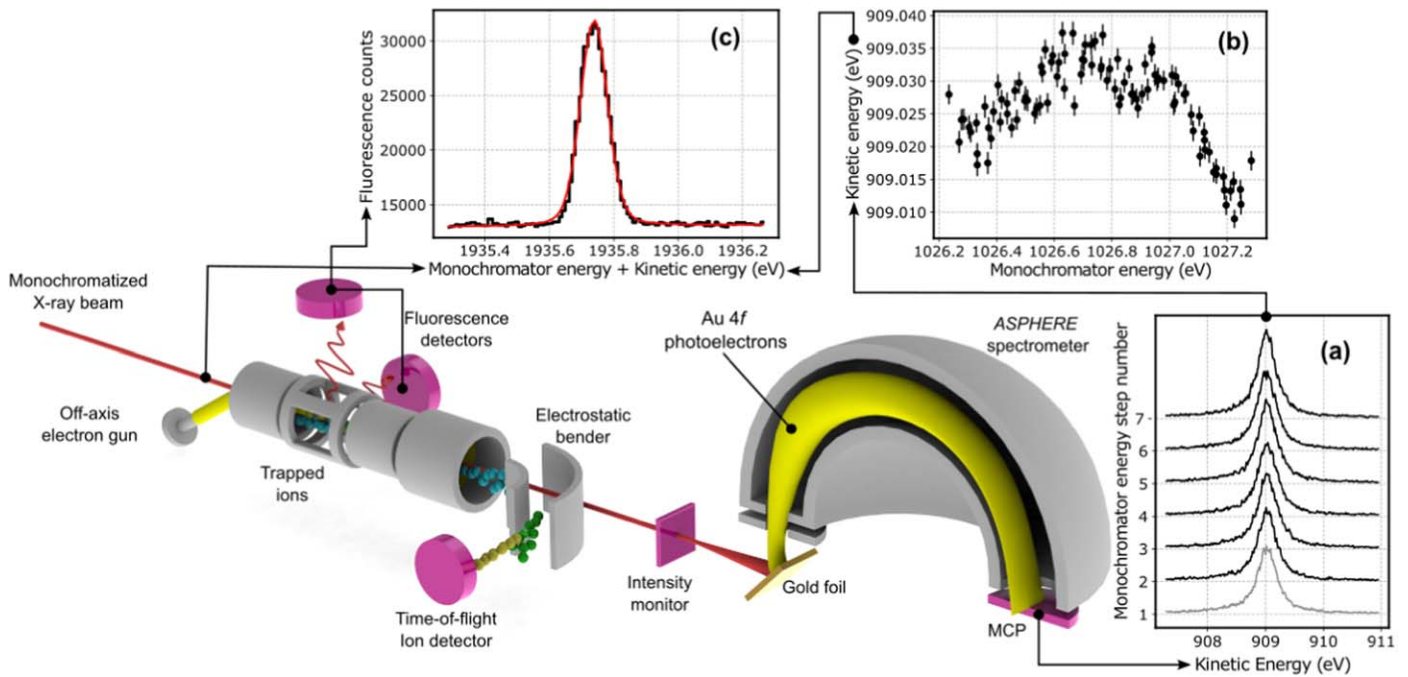


Figure 1. A photon beam of variable energy excites an elongated ion ensemble within a portable EBIT, PolarX-EBIT (Micke et al. 2018). Emitted fluorescence X-rays are recorded by two silicon drift detectors. Ions periodically released from the trap are mass-analyzed by their time of flight as a monitoring diagnostic of the trapped ion content. Downstream, the photon beam passes through a wire mesh used to measure its intensity before hitting a gold target and releasing photoelectrons that enter ASPHERE, a high-resolution hemispherical electron-energy analyzer. ASPHERE records (a) the Voigt-like kinetic energy distribution of Au $4f_{7/2}$ electrons and their centroids (b) at each monochromator energy step. Because we apply a bias to the Au target that tracks changes in the nominal monochromator energy, ideally, (b) is expected to exhibit constant values, but it shows small yet reproducible periodic deviations from the nominal monochromator energy scale due to interpolation errors in the angular encoders. These deviations are corrected for in (c) prior to calibration with reference lines.

of freedom removed by requiring fulfillment of the constant fix-focus condition (Follath 2001). The absolute angles of both grating and mirror are recorded using angular encoders. To measure electronic transitions with narrow natural line widths < 50 meV, angular increments as small as $\approx 10^{-5}$ degrees have to be resolved, equivalent to 36 mas or 175 nrad. The installed Heidenhain RON 905 angular encoders have 36,000 reference marks per turn, or one every 10^{-2} degrees ($36''$). Such encoders interpolate angle changes 1000 times between each mark. An LED source is positioned on one side of the disk, while two photodiodes are positioned on the opposite side of the disk to record the light intensity modulated by slight rotations of the encoder disk.¹³ These intensity variations are then stored in an empirical lookup table in the hardware. However, the process is highly sensitive to imperfections in the analog signals, which can lead to periodic subdivision errors (Follath & Balzer 2010; Krempaský et al. 2011). Furthermore, within each monochromator, there are two encoders—one dedicated to the grating and the other to the focusing mirror. This doubles the uncertainty in the interpolation, impacting the determination of the diffraction angle. Consequently, this can cause the nominal monochromator energy to deviate from the actual photon beam energy. This problem was previously observed in our studies at P04 (Kühn et al. 2022; Togawa et al. 2023) and other beamlines (Follath & Balzer 2010; Krempaský et al. 2011), and leads to periodic fluctuations in the nominal photon-energy scale, which in our case have peak-to-peak amplitudes of up to ~ 50 meV below 900 eV and ~ 70 meV above 900 eV.

To correct for them while scanning the monochromator to excite resonant transitions, we direct the photon beam exiting the EBIT onto a gold target mounted on a high-resolution hemispherical electron-energy analyzer, ASPHERE (Rosnagel et al. 2001), as shown in Figure 1. There, $4f_{5/2,7/2}$ photoelectrons are emitted, and their kinetic energy is measured. The kinetic energy of these photoelectrons is given by the difference between the photon energy and the binding energy of the electrons, along with any potential bias applied to the gold target. If the bias potential applied to the target is constant, any change in the photon energy will manifest itself as a change in the kinetic energy of the $4f$ Au electrons. However, if we change the target bias to track changes in the nominal photon energy, the electron kinetic energy remains nominally constant and the photoelectron peak (Au $4f_{7/2}$) can appear at a fixed position on the electron detector, see Figure 1(a). Thus, any deviation of the actual photon energy from the nominal photon energy set by the monochromator would result in a deviation of the kinetic energy of the photoelectrons. An example of such a deviation, reflecting the interpolation inaccuracies of the two angular encoders of the monochromator, is shown in Figure 1(b). We fit Au $4f_{7/2}$ peaks (line widths of about 700 meV FWHM) with Voigt profiles to find their centroids and determine their kinetic energies with uncertainties of a few meV at electron count rates of $\sim 10^4$ s $^{-1}$. By cooling the gold target to liquid nitrogen temperature, we further reduce the peak width to ~ 450 meV, which further improves centroid determination. We then use this information to correct each step of the nominal monochromator energy scale. To avoid any assumptions in modeling these deviations shown in Figure 1(b), and because the addition of an arbitrary constant term to the energy scale will be removed when calibrating against

¹³ https://www.heidenhain.us/wp-content/uploads/2022/07/591109-24_Angle_Encoders_with_Integral_Bearing.pdf

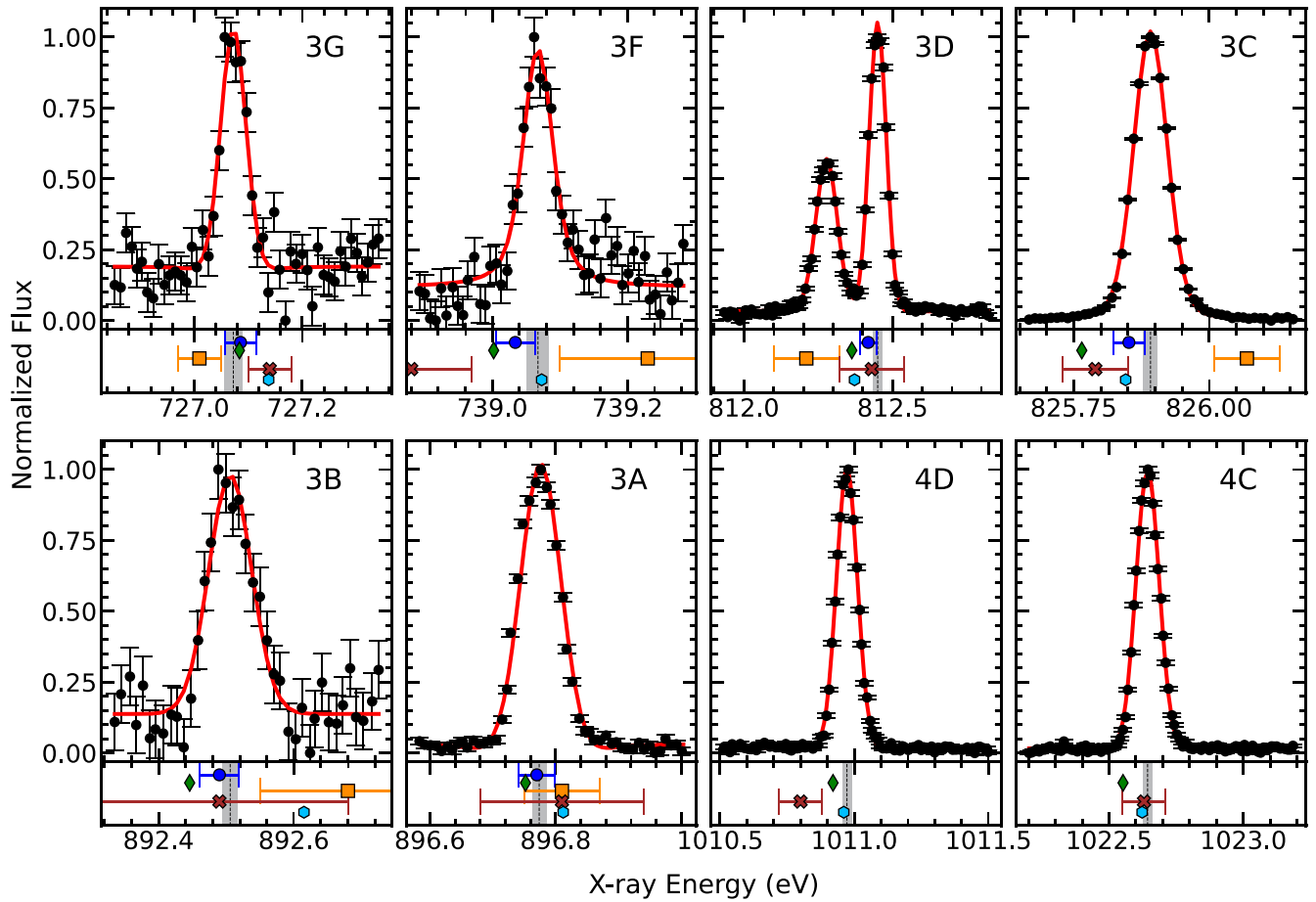


Figure 2. (Top panels) Representative scan for each of the measured Fe XVII lines. Both the data and model are scaled to the range [0,1]. (Bottom panels) Measured transition energies derived from a weighted average of all scans are depicted with their total uncertainty represented by the gray band. They are compared against Large CI (blue circles), FAC MBPT (green diamonds), solar observations (cyan hexagons), and previous laboratory data (orange squares: Beiersdorfer & Wargelin 1994; brown crosses: Brown et al. 1998).

known reference energies, we simply add the measured electron kinetic energy directly to the nominal monochromator energy scale rather than first subtracting a nominal kinetic energy offset. On this corrected monochromator energy scale (Figure 1(c)), we then determine the centroids of the calibration lines and associate them with the theoretical references mentioned above. By fitting a third-order polynomial to these data, we obtain the dispersion curve and thus the calibrated monochromator energy scale.

For the Fe XVII measurements, we set the EBIT to use a ~ 4 mA, 3500 eV electron beam, capable of directly exciting the lines studied here, and thus generating an undesired background. These parameters yielded a ratio of photoexcitation peak to electron-impact background between 2 and 3 throughout the experiment, indeed lower than the ratio of ≈ 45 achieved in our previous work (Kühn et al. 2022) by cyclically switching the electron-beam energy between ion breeding and probing energy after a long parameter optimization. This time, since switching tests showed a severe loss of Fe XVII ions, we decided to use a constant electron-beam energy of 3500 eV, well above that of dielectronic recombination satellites. The present signal-to-noise ratio and resolving power of 13,000 were sufficient for our reported accuracy.

The P04 monochromator was scanned over ranges covering $3s - 2p$ (3G and 3F), $3d - 2p$ (3C and 3D), $3p - 2s$ (3A and 3B), and $4d - 2p$ transitions (4C and 4D) of Fe XVII.

Fluorescence was collected in the SDDs for 10–15 s at each monochromator step. The count rate for each transition is directly proportional to the respective oscillator strength, and we can see transitions with excitation rates about 4–80 times lower than that of the 3C transition. Scans of each line were therefore repeated as needed to obtain good statistics. This also yielded adequate statistics at each step for the Au $4f_{7/2}$ photoelectron peak position determination needed for the nominal monochromator photon-energy scale correction. To construct the spectrum for a single transition, as depicted in Figure 2, all photons detected in the SDDs within a 50 eV region of interest centered around the expected energy are summed as a function of the monochromator energy. A representative scan for each of these lines is shown in Figure 2. The transition energies of the Fe XVII lines were determined using a maximum-likelihood fit of Voigt profiles added to the linear background term arising from electron-impact excitation using the cash statistic (Cash 1979; Kaastra 2017). The Voigt function is a convolution of Lorentzian and Gaussian functions. The Gaussian contributions to the line width arise from the limited resolution of the monochromator and the thermal motion of the ions (Hoesch et al. 2022). The Lorentzian width, as shown in Kühn et al. (2022), stems from the natural line width of the transition and a pseudo-Lorentz instrumental component due to X-ray diffraction at beamline components (Follath & Balzer 2010). Given the possible energy-dependent

Table 1

Experimental and Calculated Transition Energies from This Work in Comparison with Previous Experiments, Astrophysical Observations, and Other Predictions

Line	Term	Configuration	This Work			Previous Experiments		Observations	
			Experiment	Large CI ^a	FAC-MBPT ^b	BW94 ^c	B98 ^d	Hinode ^e	SMM ^f
3G	3P_1	$[1s^2 2s_{1/2}^2 2p_{1/2}^2 2p_{3/2}^3 3s_{1/2}]_1$	727.073(15)	727.086 (−0.013)	727.084 (−0.011)	727.01(4) (0.06)	727.14(4) (−0.06)	727.14 (−0.06)	727.14 (−0.06)
3F	1P_1	$[1s^2 2s_{1/2}^2 2p_{1/2}^2 2p_{3/2}^4 3s_{1/2}]_1$	739.067(15)	739.034 (0.033)	739.002 (0.065)	739.23(13) (−0.17)	738.88(9) (0.19)	739.07 (−0.01)	739.10 (−0.03)
3D	3D_1	$[1s^2 2s_{1/2}^2 2p_{1/2}^2 2p_{3/2}^3 3d_{5/2}]_1$	812.417(13)	812.418 (−0.001)	812.363 (0.054)	812.21(11) (0.21)	812.43(11) (−0.01)	812.37 (0.05)	812.74 (−0.33)
3C	1P_1	$[1s^2 2s_{1/2}^2 2p_{1/2}^2 2p_{3/2}^4 3d_{3/2}]_1$	825.870(12)	825.852 (0.019)	825.765 (0.106)	826.07(6) (−0.20)	825.79(6) (0.08)	825.85 (0.02)	825.90 (−0.03)
3B	3P_1	$[1s^2 2s_{1/2}^2 2p_{1/2}^2 2p_{3/2}^6 3p_{1/2}]_1$	892.496(10)	892.490 (0.007)	892.446 (0.050)	892.68(13) (−0.18)	892.49(19) (0.01)	892.61 (−0.12)	892.61 (−0.12)
3A	1P_1	$[1s^2 2s_{1/2}^2 2p_{1/2}^2 2p_{3/2}^6 3p_{3/2}]_1$	896.774(10)	896.770 (0.004)	896.752 (0.022)	896.81(6) (−0.04)	896.81(13) (−0.04)	896.81 (−0.04)	896.88 (−0.10)
4D	3D_1	$[1s^2 2s_{1/2}^2 2p_{1/2}^2 2p_{3/2}^4 4d_{5/2}]_1$	1010.983(16)	...	1010.921 (0.062)	...	1010.80(8) (0.19)	1010.96 (0.02)	1011.04 (−0.06)
4C	1P_1	$[1s^2 2s_{1/2}^2 2p_{1/2}^2 2p_{3/2}^4 4d_{3/2}]_1$	1022.639(16)	...	1022.552 (0.087)	...	1022.63(8) (0.01)	1022.62 (0.02)	1022.80 (−0.16)

Notes. All values in eV. Values in parentheses following the measured values give total uncertainties and parentheses below the measured values indicate absolute differences from the present measurements.

^a Large CI calculations, method is from Cheung et al. (2021).

^b CI + second-order MBPT of FAC, method is from Gu et al. (2006).

^c EBIT measurements by Beiersdorfer & Wargelin (1994).

^d EBIT measurements by Brown et al. (1998).

^e Solar observations by Hinode: Del Zanna & Ishikawa (2009).

^f Solar observations by SMM: Phillips et al. (1982).

contributions to line widths from beamline components, we chose to leave all parameters of the Voigt profile unconstrained during our fitting procedure for determining the line centroids.

Table 1 presents the results for eight Fe XVII lines and their associated uncertainties from errors in the centroid determination of calibration lines, the dispersion fit 1σ confidence band, and the centroid determination of each Fe XVII line, which is typically in the range of 1–3 meV. The total systematic uncertainties of the calibration are estimated to reach levels of 10–15 meV. As mentioned before, the angular encoder interpolation error induces oscillations of the nominal monochromator photon energy scale up to ± 70 meV in the 650–1150 eV energy range. While accurate reference energies and the corrections from ASPHERE to the photon-energy axis help mitigate these oscillations, $\sim 10\%$ – 20% (7–14 meV) residual variations still remain in the corrected monochromator photon-energy scale. A potential source of these could be the limited resolution of the Keithley 6517 voltage source biasing the gold target. Despite using a seven-digit calibrated voltmeter (Agilent 3458a), the voltage source operates in 5 mV steps within the 100 V range, limiting our electron kinetic energy measurements. Further systematics arise from the frequent switching of the voltage range of this bias supply needed to cover the monochromator range of 600–1150 eV, requiring separate calibration for each voltage range. Unfortunately, we could only calibrate the bias supply in a narrow 20 V range. Moreover, unmeasured fluctuations in the voltages applied to the inner and outer hemispheres of the electron spectrometer may have introduced additional systematic uncertainties. The dimensional stability of its electron-optics components is affected by thermal drifts caused by varying ambient conditions at ppm levels to which we are already sensitive. Note that we

also fit our data with skewed Voigt profiles, allowing for a nonzero skewness, thus accounting for any line asymmetries that may exist due to monochromator imperfections (Perry-Sassmannshausen et al. 2021; Hoesch et al. 2022; Togawa et al. 2023). These tests resulted in changes to the line centroids of less than ~ 1 meV, which is negligible considering the total uncertainty of our measurements. We considered whether lines from contaminant ions of oxygen, fluorine, or neon originating from residual calibration gases could lead to systematic errors in any of our transition-energy determinations. Because these lines have known transition energies, and because of the extremely high resolving power (13,000) attained in our experiment, we ruled out any significant effect from such contamination. After conservatively considering all these sources, our present uncertainties are a factor of 4–20 smaller than those of previously reported experiments (Beiersdorfer & Wargelin 1994; Brown et al. 1998).

3. Discussion of the Results

We compare the present results in Figure 2 and Tables 1 and 2 with earlier experimental data, observations, and predictions, including our own. Our calculations employ the latest version of our highly scalable parallel CI code (Cheung et al. 2021; see Appendix). Optimization of the basis-set construction allowed faster convergence with the principal quantum number n than in our prior work (see supplementary material of Kühn et al. 2022) while including higher partial waves (h , i , and k), and a larger number of reference configurations of even and odd parity. Table 3 shows the QED and other contributions in cm^{-1} for the measured transitions. Column 17g shows the results obtained with the $17spdfg$ basis set (see the Appendix A);

Table 2
Continuation of Table 1

Line	Large CI ^a (old)	Exp. ^b	NIST ASD ^c	AtomDB ^d CI	CHIANTI ^e MRMP	CHIANTI ^f AS	SPEX ^g	W16 ^h MBPT	S15 ⁱ MBPT	G05 ^j MBPT	A04 ^k MCDF
3G	726.97 (0.10)	727.11 (−0.03)	727.14 (−0.07)	725.79 (1.28)	727.06 (0.01)	727.48 (−0.41)	727.18 (−0.11)	726.78 (0.29)	...	727.12 (−0.05)	725.38 (1.70)
3F	738.91 (0.16)	739.04 (0.03)	739.05 (0.01)	738.01 (1.06)	739.00 (0.07)	738.21 (0.85)	738.88 (0.19)	738.72 (0.34)	...	739.06 (0.01)	736.05 (3.02)
3D	812.32 (0.10)	812.41 (0.01)	812.37 (0.05)	811.70 (0.72)	812.41 (0.01)	813.65 (−1.23)	812.48 (−0.06)	812.04 (0.37)	812.57 (−0.15)	812.44 (−0.02)	811.08 (1.34)
3C	825.76 (0.11)	825.83 (0.04)	825.70 (0.17)	825.83 (0.04)	825.76 (0.11)	827.52 (−1.65)	826.01 (−0.14)	825.39 (0.48)	825.89 (−0.02)	825.70 (0.17)	825.01 (0.86)
3B	892.50 (−0.00)	894.25 (−1.75)	892.41 (0.08)	895.55 (−3.05)	892.61 (−0.12)	892.21 (0.29)	...	892.40 (0.10)	894.25 (−1.75)
3A	896.90 (−0.13)	898.54 (−1.77)	896.67 (0.10)	899.85 (−3.08)	897.14 (−0.36)	896.46 (0.31)	...	896.62 (0.15)	898.55 (−1.77)
4D	1011.00 (−0.02)	1009.79 (1.19)	...	1012.03 (−1.05)	1011.29 (−0.31)	1010.53 (0.46)	1009.22 (1.76)
4C	1022.70 (−0.06)	1021.76 (0.88)	...	1023.64 (−1.00)	1022.97 (−0.33)	1022.17 (0.47)	1020.90 (1.74)

Notes. The experimental results are compared with previous predictions, with energy units expressed in eV. Values in parentheses below the predicted values denote the absolute differences from the current measurements.

^a Large CI: Kühn et al. (2022).

^b Preliminary critical analysis of Fe XVII spectral data, A. Kramida (2019, private communication).

^c NIST Atomic Spectroscopy Database: Kramida et al. (2022).

^d AtomDB Database: Loch et al. (2006; APED: `fe_17_LV_v3_0_4_a.fits`).

^e Chianti Database with MRMP calculations: Del Zanna & Ishikawa (2009).

^f Chianti Database with AS calculations: Liang & Badnell (2010).

^g SPEX database: Gu et al. (2020).

^h MBPT by Wang et al. (2016).

ⁱ MBPT by Santana et al. (2015).

^j MBPT by Gu (2005).

^k MCDF by Aggarwal et al. (2003).

Table 3

Contributions to the Theoretical Energies (in cm^{-1} above the Ground State) of Fe XVII from an Enlarged Basis Set ($>17g$), Additional Reference Configurations (Extras), and QED in Comparison with Our Measurements and Their Errors in cm^{-1}

Label	This Exp.	Error	$\Delta\text{Prev. Th.}^a$	17g	$\geq 17g$	Extras	QED	Final	$\Delta\text{This Th.}^b$	$\Delta\text{This Th.}^b$ (%)
3G	5,864,241	122	841	5,862,842	541	146	814	5,864,343	−102	0.0017
3F	5,960,976	123	1274	5,958,941	558	146	1067	5,960,711	265	0.0045
3F–3G	96,736	174	434	96,099	17	0	253	96,368	368	0.3800
3D	6,552,587	103	787	6,552,044	294	104	151	6,552,594	−7	0.0001
3C	6,661,093	96	897	6,660,390	248	5	299	6,660,942	151	0.0023
3C–3D	108,506	141	110	108,346	−46	−99	148	108,348	158	0.1454
3B	7,198,469	82	...	7,200,865	573	−28	−2993	7,198,416	53	0.0007
3A	7,232,969	82	...	7,235,357	547	−8	−2958	7,232,938	31	0.0004
3A–3B	34,500	116	...	34,492	−25	20	35	34,522	−22	0.0626

Notes. Note that we used the CODATA2018 (Tiesinga et al. 2021) recommended value of hc to convert experimental values from eV to cm^{-1} . The difference between the three pairs of lines is shown in bold.

^a This column shows the difference between previous theoretical large CI computations from Kühn et al. (2022) and those of the present experiment.

^b This column shows the difference between current theoretical large CI computations and those of the present experiment.

column $>17g$, additional contributions from highly excited orbitals up to $24spdfgh21i17k$; “Extras,” additional contributions due to the much larger number of configurations included in CI, selected to give the large contributions. The final results are the sum of these three columns and a QED contribution (Tupitsyn et al. 2016). Column [$\Delta\text{This Th.}$] shows differences between the current experiment and theory, and column [$\Delta\text{Prev. Th.}$] shows differences from previous calculations presented in Kühn et al. (2022), demonstrating a

significant improvement. We estimate the uncertainty in the electronic correlation computations to be approximately 29 meV ($\sim 230 \text{ cm}^{-1}$), primarily arising from the $>17g$ contribution (see Appendix A). The difference between theory and experiment is within the combined uncertainties for all six levels. This allows us to estimate the uncertainty of the QED contribution at 30–32 meV ($240\text{--}260 \text{ cm}^{-1}$), which is the combined theory and experimental uncertainties added in quadrature. We also computed the energies of the 3A and 3B

levels for the first time. The $2s - 3p$ lines (3A and 3B), which involve a $2s$ electron, have the largest QED contributions (~ 370 meV, or ~ 3000 cm $^{-1}$), while for $3s - 2p$ transitions 3G and 3F as well as $3d - 2p$ ones (3C and 3D) they are much smaller. From the 3A and 3B results, we thus estimate a relative QED accuracy of 8%.

As shown in Table 1, line 3F, close to the He-like $F K\alpha$ calibration line, shows a larger absolute deviation of about 33 meV from the large CI prediction, while the remaining measured lines remain below ~ 10 – 20 meV. Unfortunately, line 3F was measured only once, unlike the others, which were scanned at least four to five times. We explored several plausible explanations for the 3F discrepancy. One possible source of the discrepancy could be the simultaneous excitation of high- n Rydberg lines of O VII within the scan range of line 3F, which could lead to a shift of the 3F centroid. Furthermore, we considered lines from the lower charge states, Fe X, Fe VIII, and Fe VII, which fall within the 3F scan range. Despite the relatively low abundance of these charge states in our experiment, they can potentially influence the 3F line due to their strong oscillator strengths. Although the theoretical line positions and oscillator strengths of these low charge states are calculated by Gu et al. (2006), they have never been compared experimentally, making it difficult to estimate their influence on the 3F position. We also investigated the possibility of magnetically induced mixing of the $J=0$ and $J=1$ ($2p_{1/2}^{-1} 3s_{1/2}$) excited states (Beiersdorfer et al. 2003), which might shift the energy of the $J=1$ state sufficiently to introduce a systematic error in our measurement of 3F. However, measurements by Beiersdorfer et al. (2016) show a separation of ~ 1.2 eV between these states, making strong magnetic-field-induced mixing unlikely. We performed FAC calculations for atoms in strong magnetic fields to verify this, finding shifts on the order of 10μ eV for the field strength in PolarX-EBIT, demonstrating that this effect is not important in our experiment. The decrease in reflectivity of the platinum-coated diffraction grating over the 3F scan range could slightly affect the centroid position determination at 739 eV. Based on simulations we estimate this effect to be smaller than 0.1 meV.

We also consider the differences between the three line pairs, as they are more sensitive to QED effects than absolute energies. Table 3 shows that the largest uncertainty, caused by the uncertainty in the basis-set convergence, is common to each of the pairs. This significantly reduces the uncertainty of electronic correlations to better than 6 meV (50 cm $^{-1}$) for the energy difference. Both (3A–3B) and (3C–3D) are in excellent agreement with our present as well as previous predictions (Kühn et al. 2022). For (3G–3F), the deviation is 46 meV (about 2σ) and can be attributed to the factors discussed above for line 3F. It is interesting to note that our measured 3F energy is in much better agreement with solar observations (Phillips et al. 1982; Del Zanna & Ishikawa 2009) than with our calculations. Nevertheless, our present calculations of the ground state transitions show an order of magnitude smaller deviation from our experimental results compared to our prior predictions (Kühn et al. 2022). This represents a benchmark with our experimental data at the level of 10–20 ppm, an unprecedented agreement for a neon-like system to the best of our knowledge.

Besides CI, we performed calculations using a combination of conventional CI and second-order many-body perturbation theory (MBPT) with the Flexible Atomic Code (FAC;

Gu 2008). Details of this method are described in Gu (2005), Gu et al. (2006), and recently in Steinbrügge et al. (2022). In these calculations, we included frequency-dependent generalized Breit interactions (Breit 1929) in both the CI expansion and the MBPT corrections, as well as self-energy and vacuum polarization calculated using the QED operator model of Shabaev et al. (2018). These predictions demonstrate a reasonable agreement with our experimental data, with the largest discrepancy of about 100 meV observed for line 3C. We compared our results with other CI+MBPT data available in the literature (Gu 2005; Santana et al. 2015; Wang et al. 2016), showing maximum deviations of up to 0.5 eV. The origin of the discrepancy between our CI+MBPT calculations and the previously published ones is unclear. We have also observed departures from the predictions of multiconfiguration Dirac–Fock (MCDHF) and autostructure (AS) calculations (Aggarwal et al. 2003; Loch et al. 2005; Liang & Badnell 2010), with deviations reaching up to 1–3 eV. However, we note that the atomic structures used in these calculations were necessarily small to facilitate their use in R-matrix collision calculations, which are computationally more demanding compared to atomic structure calculations. Other accurate predictions for Fe XVII from multireference Møller–Plesset (MRMP) are reported in Del Zanna & Ishikawa (2009) and included in the CHIANTI code. They show very good agreement with our experimental data.

We compare our results with laboratory data from Beiersdorfer & Wargelin (1994) and Brown et al. (1998). Both works measured electron-impact spectra of Fe XVII under similar experimental conditions in the Lawrence Livermore National Laboratory EBIT facility using a crystal spectrometer employing a cesium acid phthalate crystal for the wavelength range of the lines presently discussed. Both measurements have carefully concatenated several spectra from different wavelength ranges and calibrated them against reference lines of hydrogenic and helium-like oxygen, fluorine, and neon, similar to our work. Nevertheless, these two measurements are themselves marginally inconsistent with each other within their quoted uncertainties. Furthermore, we find that our measurements are also marginally inconsistent with both these previous measurements within uncertainties. The source of these marginal inconsistencies is unknown.

We also compare our results with data from widely used databases and plasma codes. The NIST Atomic Spectroscopy Database (ASD; Kramida et al. 2022) values showed significant deviations for lines 3C and 3A. However, when critically evaluated $n = 3 - 2$ data by the authors of the NIST ASD (A. Kramida 2019, private communication) were considered, we found a much better agreement with our experimental results (see Table 2). Comparison with AtomDB (Foster et al. 2012), CHIANTI (Del Zanna et al. 2021), and SPEX (Kaastra et al. 1996) databases and plasma codes revealed discrepancies as large as 1–2 eV. SPEX numbers showed better agreement with our results than those found in AtomDB, since SPEX has updated Fe-L atomic data (Gu et al. 2019, 2020, 2022), which were mainly calculated using FAC. Although the Astrophysical Plasma Emission Database (APED) version in AtomDB shows different values in its online webguide version (2.0.1)¹⁴ and its pyatomdb version (3.0.4), the theoretical source is in both cases Loch et al. (2005), which uses the CI method, and disagrees by up to

¹⁴ <http://www.atomdb.org/Webguide/webguide.php>

1–2 eV from our results, as shown in Table 2. CHIANTI provides two sources for the energies: AS theory (Liang & Badnell 2010), and the more accurate set of data from MRMP theory (Del Zanna & Ishikawa 2009). Note that the theoretical energy level data in AtomDB and Chianti are not used when generating model spectra when more accurate experimental or observational values exist. AtomDB replaces the most important transition energies of Fe XVII with the Brown et al. (1998) values, whereas CHIANTI uses the observed transition energies from solar observation (Del Zanna & Ishikawa 2009).

Overall, most experimental and observational data agree with our experiment within 0.1 eV on average, well within the error bars of earlier works. However, there are substantial discrepancies with predictions from certain theoretical models, exceeding the margins of error associated with the experimental results. This highlights the urgent need to update the aforementioned databases to avoid pitfalls in astrophysical spectrum modeling and interpretation of observational data.

4. Summary and Conclusions

We presented high-precision transition-energy measurements of eight strong, astrophysically preeminent Fe XVII transitions required for plasma diagnostics. Our approach combined resonant photoexcitation of Fe XVII and narrow H-like and He-like transitions with high-resolution photoelectron spectroscopy (Rosnagel et al. 2001). This eliminates a very common source of systematic errors found even in advanced monochromators, namely quasiperiodic encoder interpolation errors (Follath & Balzer 2010; Krempaský et al. 2011). As a result, our Fe XVII measurements represent a significant improvement in accuracy compared to previous experimental references, achieving an average enhancement of almost an order of magnitude. The uncertainties now stand at 10–15 meV, which translates to Doppler shifts of approximately $\pm 5 \text{ km s}^{-1}$. A further improvement in accuracy by another order of magnitude will require incorporating high-resolution/high-stability voltage sources and more accurate voltmeters at ASPHERE to eliminate systematic errors associated with knowledge of the bias voltages.

We have also improved our high-precision calculations by an order of magnitude in comparison with previous best calculations (Cheung et al. 2021; Kühn et al. 2022). This improvement allowed us, for the first time, to test the accuracy of QED corrections to the transition energies of a complicated 10-electron system. We expect that the achieved QED accuracy is applicable to a broad range of ions of intermediate degrees of ionization that can be treated with our large-scale CI or CI+all-order approaches. This has significant implications for predicting energy levels in systems where no experimental data are available for a wide range of applications in astrophysics, plasma physics, and atomic clock development (King et al. 2022). The established QED accuracy is deemed sufficient for high-precision prediction of HCI clock transitions (Kozlov et al. 2018). Improved accuracy of the experimental values would allow us to further decouple the uncertainty due to basis-set convergence from the uncertainty in the QED and improve theory predictions.

Our improved transition-energy measurements for Fe XVII are sufficiently accurate that the uncertainties are no longer a significant part of the error budget for present or future planned astrophysical instruments, such as Chandra HETGS, XMM-Newton RGS, XRISM (Tashiro et al. 2018), Athena (Pajot et al. 2018), LEM (Kraft et al. 2022), HUBS (Cui et al. 2020),

Arcus (Heilmann et al. 2022), HiReX (Nicastro et al. 2021), and Lynx (Schwartz et al. 2019). Future campaigns of similar measurements of prominent transitions in key ions (especially Fe-L shell ions) would be of great utility and could easily be directly included in commonly used astrophysical plasma spectral databases.

The closeness of our large CI calculations to our measured values, with the worst deviation at line 3F of 33 meV amounting to a Doppler shift of only 13 km s^{-1} , shows that such well-converged calculations are sufficiently accurate to be readily used in spectral databases. While there is no reason for this in the case of the lines measured in the present work, when accurate measurements are not available, similarly well-converged results could be used for other transitions of Fe XVII and many other ions. By including a very large number of configurations, our agreement becomes significantly better than that of other well-performing methods, such as results from less-converged large CI, MBPT, and MRMP calculations. For Fe XVII, our calculations are more accurate than even the best measurements for Fe-L shell transitions in Li-like through F-like ions (Brown et al. 2002). This suggests a near-future research program composed of comprehensive large CI calculations of transition energies for all ions of astrophysical interest up to Ne-like, supplemented by targeted experiments aimed at measuring the most important transition energies.

Acknowledgments

This research was funded by the Max Planck Society (MPG) and the German Federal Ministry of Education and Research (BMBF) under project 05K13SJ2. C.S. acknowledges support from NASA under grant No. 80GSFC21M0002 and MPG. F.S. P. and M.A.L. acknowledge support from the NASA Astrophysics Program. The theoretical work has been supported by the US NSF grants Nos. PHY-2012068 and PHY-2309254 and US Office of Naval Research grant No. N00014-20-1-2513. Calculations were performed in part using the computing resources at the University of Delaware, in particular the Caviness and DARWIN high-performance computing clusters. M.S.S. thanks MPIK for the hospitality. We thank DESY (Hamburg, Germany), a member of the Helmholtz Association HGF, for the provision of experimental facilities. Parts of this research were carried out at PETRA III. We thank the P04 team at PETRA III for their skillful and reliable work. We also thank the anonymous referees whose comments and suggestions helped improve and clarify this manuscript.

Appendix A Large-scale CI Calculations

In this work, we conducted extensive high-precision calculations of Fe XVII. We start from the solution of the Dirac–Hartree–Fock equations in the central field approximation to construct the one-particle orbitals. Calculations are carried out using a CI method, correlating all 10 electrons. Breit interaction is included in all calculations. QED corrections are taken from the previous work (Kühn et al. 2022) except for the levels with a $2s$ hole, which were not computed in 2022. The same method is used in all QED calculations (Tupitsyn et al. 2016). The CI wave function is obtained as a linear combination of all distinct states of a given angular momentum

J and parity:

$$\Psi_J = \sum_i c_i \Phi_i. \quad (\text{A1})$$

The low-lying energies and wave functions are determined by solving the time-independent multielectron Schrödinger equation

$$H\Phi_n = E_n\Phi_n. \quad (\text{A2})$$

Expanding the previous work (Kühn et al. 2022), we perform several calculations optimizing the basis-set convergence, including higher partial waves up to k orbitals, and significantly expanding the set of reference configurations until convergence is reached in these parameters as well.

We have shown a comparison of our theoretical results for six transitions measured in this work with the experiment in the main text. We note that such a larger-scale computation of the 4C and 4D levels is beyond the capabilities of available computational resources (32 TB of memory and about 2000 CPUs on our largest available partition). Computing higher-lying levels requires computing of all the lower-lying levels with the same angular momentum and parity, drastically increasing memory requirement.

To test the consistency of our approach, we compare the data for the even and larger number of odd levels in Table 4 with the preliminary critical analysis of Fe XVII spectral data by A. Kramida (2019, private communication). These data generally agree well with our experiment (except for levels with a $2s$ hole), so they serve as a good general reference for other levels. The six levels measured in this work are shown in bold. The final values are given in cm^{-1} in Table 4 in the column “Final.” The difference between the final values and the experimental values in cm^{-1} and percentage are given in the last two columns.

We will discuss a complete assessment of the main contributions to the energies, including the basis-set construction, the inclusion of extra configurations, and QED. We find excellent agreement with experiments for all energies, at the level of 0.0004% for some levels. With the high level of accuracy attained, we are able to test QED contributions in the calculations of multielectron systems for the first time.

Computation. We consider Fe XVII as a system with 10 valence electrons and start with all possible single and double excitations to any orbital up to $17spdfg$ from the $1s^22s^22p^6$ and $1s^22s^22p^53p$ even-parity reference configurations, and the $1s^22s^22p^53s$, $1s^22s^22p^53d$, and $1s^22s2p^63p$ odd-parity reference configurations. For example, a single excitation from the reference configurations $2s^22p^6$ can include promoting an electron from the $2s$ or $2p$ orbitals to any orbital up to $17s$, $17p$, ... $17g$, with $2s^22p^510p$ or $2s2p^617s$ as example outcomes. We designate the basis set by the highest principal quantum number and the highest partial wave included. For example, $17g$ means that all orbitals up to $n = 17$ are included for $spdfg$ partial waves. Note that $1s^2i$ is removed from all the designations to save space.

The base calculation for the energy levels is done with a $17g$ basis set and is listed in cm^{-1} in Table 4 in column “ $17g$.” The contributions to the energy levels from expanding the basis set to $20g$ and $24g$ are in the columns “ $+20g$ ” and “ $+24g$,” respectively. The largest difference between the $23g$ and $24g$ calculations was 3 cm^{-1} , so the basis set at the level of $spdfg$ partial waves is considered sufficiently saturated. We note that although the $24spdfg$ basis was also used in Kühn et al. (2022),

we constructed a more compact basis in the present work, to significantly improve convergences with the principal quantum number n . The basis is constructed in the 5 a.u. cavity, while the basis in Kühn et al. (2022) was constructed in a 20 a.u. cavity, with additional differences in the constructions of the higher partial-wave orbitals. A detailed comparison of the two computations confirms much better convergence properties of the present basis. We note very large computational resources needed for a basis-set expansion, especially for the inclusion of higher partial waves.

Contributions to higher partial waves are considered in the next six columns of Table 4. We calculated the contributions of extending the base $17g$ basis set to include up to $17h$ orbitals and listed them in column “ $+17h$.” Next, we successively increase the principal quantum number and increase the basis set up to $24h$. The contributions from (18 to 20) h orbitals and (21–24) h orbitals are given in columns “ $+20h$ ” and “ $+24h$,” respectively. The largest difference between $23h$ and $24h$ calculations was 9 cm^{-1} , so the energies of including the higher h orbitals have also converged sufficiently. We note that a large fraction of the nh contribution comes from very high- n orbitals, so the inclusion of the first few h orbitals does not give correct results for this partial wave. This effect is exacerbated for the i and k orbitals, where more of the contribution is expected to come from $n > 20$ even with the present compact basis.

The same procedure was used to obtain contributions from the i orbitals up to $21i$ and k orbitals up to $17k$ and are listed under columns “ $+21i$ ” and “ $+17k$,” respectively. Contributions from including i orbitals up to the same principal quantum number $n = 17$ as the base run are listed in column “ $+17i$.” Due to the high computational demand for higher partial-wave calculations, we did not perform calculations for odd-parity states at the level of $21i$. Instead, we set the contributions of $21i$ to the odd-parity energies to be the average of the even-parity state contributions, which was 81 cm^{-1} . Contributions from k orbitals were already at a level of convergence around 15 cm^{-1} at $21i$.

We note that we have performed detailed convergence studies computing a separate contribution for each nl for the last few principal quantum numbers to evaluate convergence. Based on these data, we conservatively estimate the missing higher g orbital contribution at 5 cm^{-1} , higher h orbital contribution at 20 cm^{-1} , and higher i orbital contribution at 50 cm^{-1} . It appears that $17k$ is not sufficiently converged. Table 4 shows that the contribution of all ni orbitals is about $1/2$ of the nh contribution. Conservatively assuming a similar convergence pattern for higher partial waves gives 70 cm^{-1} for the k partial wave and a similar total contribution for all the other partial waves. The total uncertainty due to the convergence of the basis set is then on the order of 230 cm^{-1} . However, we note that the incomplete convergence of the basis is expected to cause a systematic shift of data for all levels; i.e., all energy values will be larger, with some smaller variances between the levels. It is possible that the partial-wave convergence is faster and the overall shift is smaller; therefore, we only use the above estimate to make an accuracy evaluation but do not shift the theory values. We note that overall $+100 \text{ cm}^{-1}$ shift of all of our values would improve the agreement of our data with the present experiment; however, this is the level of the experimental precision at 1σ so improved

Table 4
Contributions to Fe XVII Energies Calculated with Increased Basis Sets and Number of Configurations

Configuration	Expt ^a	Δ^b	17g	+20g	+24g	+17h	+20h	+24h	+17i	+21i	+17k	QED	Extras	Final	Δ	Δ (%)	
															Present		
$2s^2 2p^6$	1S_0	0	0	0	0	0	0	0	0	0	0	0	0	0	0	0	
$2s^2 2p^5 3p$	3S_1	6,093,295	1124	6,092,365	44	20	278	58	45	64	86	8	70	107	6,093,143	152	0.002%
$2s^2 2p^5 3p$	3D_2	6,121,484	988	6,120,688	38	18	252	51	40	56	77	4	56	...	6,121,280	204	0.003%
$2s^2 2p^5 3p$	3D_3	6,134,539	1015	6,133,678	41	19	258	54	42	58	81	5	107	...	6,134,345	194	0.003%
$2s^2 2p^5 3p$	1P_1	6,143,639	1013	6,142,785	39	18	253	52	40	56	78	4	93	...	6,143,417	222	0.004%
$2s^2 2p^5 3s$	2	5,849,216	1134	5,847,527	38	16	269	52	35	63	81	8	813	149	5,849,052	164	0.003%
$2s^2 2p^5 3s$	3P_1	5,864,502	1102	5,862,842	37	15	258	50	34	60	81	7	814	146	5,864,343	158	0.003%
$2s^2 2p^5 3s$	1P_1	5,960,742	1040	5,958,941	41	18	259	55	37	60	81	7	1067	146	5,960,711	31	0.001%
$2s^2 2p^5 3d$	$^3P_0^o$	6,471,640	1148	6,470,765	51	24	138	65	47	22	81	-2	95	139	6,471,426	214	0.003%
$2s^2 2p^5 3d$	$^3P_2^o$	6,486,183	1007	6,485,436	51	24	121	65	47	17	81	-4	109	139	6,486,086	97	0.001%
$2s^2 2p^5 3d$	$^3F_4^o$	6,486,720	920	6,486,064	51	24	90	65	47	7	81	-7	105	142	6,486,669	51	0.001%
$2s^2 2p^5 3d$	$^3F_3^o$	6,492,651	856	6,492,060	50	23	66	64	46	-2	81	-10	102	138	6,492,621	30	0.000%
$2s^2 2p^5 3d$	$^1D_2^o$	6,506,537	855	6,505,941	50	23	62	64	46	-3	81	-10	107	138	6,506,500	37	0.001%
$2s^2 2p^5 3d$	$^3D_3^o$	6,515,203	807	6,514,654	50	23	49	63	46	-8	81	-12	107	136	6,515,189	14	0.000%
$2s^2 2p^5 3d$	$^3D_1^o$	6,552,503	703	6,552,044	51	24	49	65	47	-9	81	-12	151	104	6,552,594	91	0.001%
$2s^2 2p^5 3d$	$^3F_2^o$	6,594,309	802	6,593,569	55	26	71	69	50	0	81	-9	355	138	6,594,404	95	0.001%
$2s^2 2p^5 3d$	$^3D_2^o$	6,600,998	938	6,600,124	54	26	80	69	49	2	81	-8	349	137	6,600,962	36	0.001%
$2s^2 2p^5 3d$	$^1F_3^o$	6,605,185	857	6,604,381	54	26	56	69	49	-6	81	-11	363	136	6,605,198	13	0.000%
$2s^2 2p^5 3d$	$^1P_1^o$	6,660,770	574	6,660,390	54	26	11	68	49	-23	81	-17	299	5	6,660,942	172	0.003%
$2s 2p^6 3p$	$^3P_1^o$	7,199,200	...	7,200,865	47	30	248	56	38	65	81	8	-2993	-28	7,198,416	784	0.011%
$2s 2p^6 3p$	$^3P_2^o$	7,219,595	48	31	251	57	39	66	81	8	-2944	-36	7,217,197	...	
$2s 2p^6 3p$	$^1P_1^o$	7,233,292	...	7,235,357	46	30	235	54	35	61	81	6	-2958	-8	7,232,938	354	0.005%

Notes. The results are compared with the preliminary critical analysis of Fe XVII spectral data by A. Kramida (2019, private communication). All energies are given in cm^{-1} . The basis set is designated by the highest principal quantum number and the highest partial wave included. For example, 17g means that all orbitals up to $n = 17$ are included for *spdfg* partial waves. The last two columns show the differences between the present computations with A. Kramida (2019, private communication) in cm^{-1} and %, respectively. The measured transitions are highlighted in bold.

^a A. Kramida (2019, private communication).













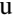



^b Kühn et al. (2022). This column shows the difference between previous theoretical large CI computations from Kühn et al. (2022) and the preliminary critical analysis of Fe XVII spectral data by A. Kramida (2019, private communication).

experimental precision is needed to definitively test the basis-set convergence.


Additionally, an extensive evaluation of the configuration weights was done to include important configurations in the list of basic reference configurations used to construct a final set of configurations. The weights of configurations signify the configuration's contribution to the corresponding wave functions and are calculated for each configuration Φ_i as $|c_i|^2$ from Equation (A1). These calculations are done by allowing single and double excitations to a much smaller 12g basis set since the size of the computational problem will become prohibitive when additional reference configurations are included. The total contributions to including these extra configurations are given in the column "Extras" in Table 4. Beyond the initial two even- and three odd-parity configurations, we systematically included an additional 12 even- and nine odd-parity reference configurations. Note that energies were calculated only for two even-parity levels to save computational resources and allow for additional reference configurations. The inclusion of these extra configurations contributes about 100 cm^{-1} shift to the energies and accounts for an additional 2 million relativistic configurations. Note also that these contributions would also be higher if the calculations were done with a larger basis set. We estimate an uncertainty from the convergence of the CI configuration set at the level of 50 cm^{-1} , which is essentially negligible in comparison with the basis-set convergence uncertainty. We note that missing contributions can be both positive and negative in this case.

Analysis of contributions to the 3F–3G, 3C–3D, and 3A–3B line differences given in the main text Table 3 shows that the basis-set expansion contribution effectively cancels for similar configurations; it is less than 50 cm^{-1} for all three cases. We also find that QED contributions play a major role in the 3F–3G energy difference. For 3C–3D, the contributions from the basis-set expansion and the addition of extra configurations essentially cancel out the QED. In the 3A–3B difference, the basis-set and extra configuration contributions cancel, leaving a shift from the QED. Therefore, comparing the differences in the energy values for similar configurations provides important additional information. It would be very useful to improve the uncertainty of the experiment as well as carry out such comparison in other ions with different degrees of ionization with 7–10 electrons.

ORCID iDs

Chintan Shah  <https://orcid.org/0000-0002-6484-3803>
 Moto Togawa  <https://orcid.org/0000-0003-4571-2282>
 Marc Botz  <https://orcid.org/0009-0003-8574-4542>
 Jonas Danisch  <https://orcid.org/0009-0002-2934-6016>
 Joschka J. Goes  <https://orcid.org/0009-0006-2461-9571>
 Sonja Bernitt  <https://orcid.org/0000-0002-1976-5121>
 Marleen Maxton  <https://orcid.org/0009-0005-9076-3101>
 Kai Köbnick  <https://orcid.org/0009-0003-0805-2438>
 Jens Buck  <https://orcid.org/0000-0002-5545-0637>
 Jörn Seltmann  <https://orcid.org/0009-0009-7545-2101>
 Moritz Hoesch  <https://orcid.org/0000-0002-0114-2110>
 Ming Feng Gu  <https://orcid.org/0000-0001-9136-8449>
 F. Scott Porter  <https://orcid.org/0000-0002-6374-1119>
 Thomas Pfeifer  <https://orcid.org/0000-0002-5312-3747>
 Maurice A. Leutenegger  <https://orcid.org/0000-0002-3331-7595>
 Charles Cheung  <https://orcid.org/0000-0002-3724-3730>

Marianna S. Safronova  <https://orcid.org/0000-0002-1305-4011>

José R. Crespo López-Urrutia  <https://orcid.org/0000-0002-2937-8037>

References

- Aggarwal, K. M., Keenan, F. P., & Msezane, A. Z. 2003, *ApJS*, **144**, 169
 Barret, D., Lam Trong, T., den Herder, J.-W., et al. 2016, *Proc. SPIE*, **9905**, 99052F
 Behar, E., Cottam, J., & Kahn, S. 2001, *ApJ*, **548**, 966
 Beiersdorfer, P., Behar, E., Boyce, K., et al. 2002, *ApJL*, **576**, L169
 Beiersdorfer, P., Bitter, M., Von Goeler, S., & Hill, K. 2004, *ApJ*, **610**, 616
 Beiersdorfer, P., Bode, M. P., Ishikawa, Y., & Diaz, F. 2014, *ApJ*, **793**, 99
 Beiersdorfer, P., Brown, G. V., & Laska, A. 2015, *JPhCS*, **583**, 012022
 Beiersdorfer, P., Crespo López-Urrutia, J. R., & Träbert, E. 2016, *ApJ*, **817**, 67
 Beiersdorfer, P., Hell, N., & Lepson, J. 2018, *ApJ*, **864**, 24
 Beiersdorfer, P., Lepson, J. K., Gu, M. F., & Bitter, M. 2017, *ApJ*, **850**, 57
 Beiersdorfer, P., Schweikhard, L., Liebisch, P., & Brown, G. V. 2008, *ApJ*, **672**, 726
 Beiersdorfer, P., Scofield, J. H., & Osterheld, A. L. 2003, *PhRvL*, **90**, 235003
 Beiersdorfer, P., & Wargelin, B. J. 1994, *RSci*, **65**, 13
 Bernitt, S., Brown, G. V., Rudolph, J. K., et al. 2012, *Natur*, **492**, 225
 Bozzo, E., Huenemoerder, D. P., Produit, N., et al. 2023, *MNRAS*, **522**, L66
 Breit, G. 1929, *PhRv*, **34**, 553
 Brinkman, A., Behar, E., Güdel, M., et al. 2001, *A&A*, **365**, L324
 Brown, G., Beiersdorfer, P., Chen, H., Chen, M., & Reed, K. 2001a, *ApJL*, **557**, L75
 Brown, G., Beiersdorfer, P., & Widmann, K. 2001b, *PhRvA*, **63**, 032719
 Brown, G., Beiersdorfer, P., Liedahl, D., Widmann, K., & Kahn, S. 1998, *ApJ*, **502**, 1015
 Brown, G. V., Beiersdorfer, P., Chen, H., et al. 2006, *PhRvL*, **96**, 253201
 Brown, G. V., Beiersdorfer, P., Liedahl, D. A., et al. 2002, *ApJS*, **140**, 589
 Cash, W. 1979, *ApJ*, **228**, 939
 Chen, G. X., & Pradhan, A. K. 2002, *PhRvL*, **89**, 013202
 Cheung, C., Safronova, M., & Porsev, S. 2021, *Symm*, **13**, 621
 Cui, W., Chen, L. B., Gao, B., et al. 2020, *JLTP*, **199**, 502
 Del Zanna, G., Dere, K. P., Young, P. R., & Landi, E. 2021, *ApJ*, **909**, 38
 Del Zanna, G., & Ishikawa, Y. 2009, *A&A*, **508**, 1517
 den Herder, J. W., Brinkman, A. C., Kahn, S. M., et al. 2001, *A&A*, **365**, L7
 Doron, R., & Behar, E. 2002, *ApJ*, **574**, 518
 Erickson, G. W. 1977, *JPCRD*, **6**, 831
 Follath, R. 2001, *NIMPA*, **467**, 418
 Follath, R., & Balzer, A. 2010, in AIP Conf. Proc. 1234, SRI 2009, 10th Int. Conf. on Synchrotron Radiation Instrumentation, ed. R. Garrett et al. (Melville, NY: AIP), 657
 Foster, A. R., Ji, L., Smith, R. K., & Brickhouse, N. S. 2012, *ApJ*, **756**, 128
 Gillaspay, J., Lin, T., Tedesco, L., et al. 2011, *ApJ*, **728**, 132
 Grell, G. J., Leutenegger, M. A., & Shah, C. 2021, *ApJ*, **917**, 105
 Grilo, F., Shah, C., Kühn, S., et al. 2021, *ApJ*, **913**, 140
 Gu, L., Raassen, A. J. J., Mao, J., et al. 2019, *A&A*, **627**, A51
 Gu, L., Shah, C., Mao, J., et al. 2020, *A&A*, **641**, A93
 Gu, L., Shah, C., Mao, J., et al. 2022, *A&A*, **664**, A62
 Gu, M., Holczer, T., Behar, E., & Kahn, S. M. 2006, *ApJ*, **641**, 1227
 Gu, M. F. 2003, *ApJ*, **582**, 1241
 Gu, M. F. 2005, *ApJS*, **156**, 105
 Gu, M. F. 2008, *CaJPh*, **86**, 675
 Heilmann, R. K., Bruccoleri, A. R., Burwitz, V., et al. 2022, *ApJ*, **934**, 171
 Hoesch, M., Seltmann, J., Trinter, F., et al. 2022, *JPhCS*, **2380**, 012086
 Ishibashi, K., Dewey, D., Huenemoerder, D. P., & Testa, P. 2006, *ApJL*, **644**, L117
 Jansen, F., Lumb, D., Altieri, B., et al. 2001, *A&A*, **365**, L1
 Kaastra, J. S. 2017, *A&A*, **605**, A51
 Kaastra, J. S., Mewe, R., & Nieuwenhuijzen, H. 1996, 11th Colloq. on UV and X-ray Spectroscopy of Astrophysical and Laboratory Plasmas, 411
 King, S. A., Spieß, L. J., Micke, P., et al. 2022, *Natur*, **611**, 43
 Kozlov, M. G., Safronova, M. S., Crespo López-Urrutia, J. R., & Schmidt, P. O. 2018, *RvMP*, **90**, 045005
 Kraft, R., Markevitch, M., Kilbourne, C., et al. 2022, arXiv:2211.09827
 Kramida, A., Ralchenko, Y., Reader, J. & NIST ASD Team 2022, NIST Atomic Spectra Database, v5.9 (Gaithersburg, MD: National Institute of Standards and Technology), <https://physics.nist.gov/asd>
 Krempaský, J., Follath, R., Strocov, V. N., Schmitt, T., & Flechsig, U. 2011, *Proc. SPIE*, **8139**, 813 90K

- Kühn, S., Cheung, C., Oreshkina, N. S., et al. 2022, [PhRvL](#), **129**, 245001
- Kühn, S., Shah, C., Crespo López-Urrutia, J. R., et al. 2020, [PhRvL](#), **124**, 225001
- Leutenegger, M. A., Kühn, S., Micke, P., et al. 2020, [PhRvL](#), **125**, 243001
- Liang, G. Y., & Badnell, N. R. 2010, [A&A](#), **518**, A64
- Loch, S., Pindzola, M., Ballance, C., & Griffin, D. 2005, [JPhB](#), **39**, 85
- Loch, S. D., Ballance, C. P., Li, Y., Fogle, M., & Fontes, C. J. 2015, [ApJ](#), **801**, L13
- Loch, S. D., Pindzola, M. S., Ballance, C. P., & Griffin, D. C. 2006, [JPhB](#), **39**, 85
- Mauche, C. W., Liedahl, D. A., & Fournier, K. B. 2001, [ApJ](#), **560**, 992
- McKenzie, D., Landecker, P., Broussard, R., et al. 1980, [ApJ](#), **241**, 409
- Micke, P., Kühn, S., Buchauer, L., et al. 2018, [RSci](#), **89**, 063109
- Nicastro, F., Kaastra, J., Argiroffi, C., et al. 2021, [ExA](#), **51**, 1013
- Oreshkina, N. S., Cavaletto, S. M., Keitel, C. H., & Harman, Z. 2014, [PhRvL](#), **113**, 143001
- Oreshkina, N. S., Cavaletto, S. M., Keitel, C. H., & Harman, Z. 2016, [JPhB](#), **49**, 094003
- Paerels, F. B. S., & Kahn, S. M. 2003, [ARA&A](#), **41**, 291
- Pajot, F., Barret, D., Lam-Trong, T., et al. 2018, [JLTP](#), **193**, 901
- Parkinson, J. 1973, [A&A](#), **24**, 215
- Perry-Sassmannshausen, A., Buhr, T., Martins, M., et al. 2021, [PhRvA](#), **104**, 053107
- Phillips, K. J. H., Fawcett, B. C., Kent, B. J., et al. 1982, [ApJ](#), **256**, 774
- Phillips, K. J. H., Greer, C. J., Bhatia, A. K., & Keenan, F. P. 1996, [ApJL](#), **469**, L57
- Pradhan, A., & Nahar, S. 2011, *Atomic Astrophysics and Spectroscopy* (Cambridge: Cambridge Univ. Press)
- Rossmagel, K., Kipp, L., Skibowski, M., & Harm, S. 2001, [NIMPA](#), **467-468**, 1485
- Saba, J. L. R., Schmelz, J. T., Bhatia, A. K., & Strong, K. T. 1999, [ApJ](#), **510**, 1064
- Santana, J. A., Lepson, J. K., Träbert, E., & Beiersdorfer, P. 2015, [PhRvA](#), **91**, 012502
- Schmelz, J. T., Saba, J. L. R., & Strong, K. T. 1992, [ApJL](#), **398**, L115
- Schwartz, D. A., Vikhlinin, A., Tananbaum, H., et al. 2019, [Proc. SPIE](#), **11118**, 111180K
- Shabaev, V. M., Tupitsyn, I. I., & Yerokhin, V. A. 2018, [CoPhC](#), **223**, 69
- Shah, C., Crespo López-Urrutia, J. R., Gu, M. F., et al. 2019, [ApJ](#), **881**, 100
- Smith, B. W., Mann, J. B., Cowan, R. D., & Raymond, J. C. 1985, [ApJ](#), **298**, 898
- Smith, R. K., Bautz, M., Bregman, J., et al. 2022, [Proc. SPIE](#), **12181**, 121812I
- Steinbrügge, R., Kühn, S., Nicastro, F., et al. 2022, [ApJ](#), **941**, 188
- Stierhof, J., Kühn, S., Winter, M., et al. 2022, [EPJD](#), **76**, 38
- Tashiro, M., Maejima, H., Toda, K., et al. 2018, [Proc. SPIE](#), **10699**, 1069922
- Tiesinga, E., Mohr, P. J., Newell, D. B., & Taylor, B. N. 2021, [RvMP](#), **93**, 025010
- Togawa, M., Kühn, S., Shah, C., et al. 2020, [PhRvA](#), **102**, 052831
- Togawa, M., Kühn, S., & Shah, C. 2023, [PhRvL](#), submitted
- Tupitsyn, I. I., Kozlov, M. G., Safronova, M. S., Shabaev, V. M., & Dzuba, V. A. 2016, [PhRvL](#), **117**, 253001
- Viefhaus, J., Scholz, F., Deinert, S., et al. 2013, [NIMPA](#), **710**, 151
- Waljeski, K., Moses, D., Dere, K. P., et al. 1994, [ApJ](#), **429**, 909
- Wang, K., Chen, Z. B., Si, R., et al. 2016, [ApJS](#), **226**, 14
- Werner, N., Zhuravleva, I., Churazov, E., et al. 2009, [MNRAS](#), **398**, 23
- Wu, C., & Gao, X. 2019, [NatSR](#), **9**, 7463
- Xu, H., Kahn, S. M., Peterson, J. R., et al. 2002, [ApJ](#), **579**, 600
- Yerokhin, V., & Surzhykov, A. 2019, [JPCRD](#), **48**, 033104
- Yerokhin, V. A., & Shabaev, V. M. 2015, [JPCRD](#), **44**, 033103